Reconstruction of Gamma-ray Direction using Boosted Decision Trees and the *Disp* Parameter

Sreela Das, 260772871

Master of Science

Department of Physics

McGill University

Montréal, Québec

June 7, 2019

A thesis submitted to McGill University in partial fulfillment of the requirements of the degree of Master of Science

Acknowledgments

I would like to thank my supervisor, Prof. Kenneth Ragan for his guidance, advice and feedback for this work. I would also like to thank Tony Lin, for his work on the analysis package that enabled the work in this thesis. Thanks are also due to Prof. David Hanna, Benjamin Zitzer, Thomas Rosin, Matthew Lundy, Emma Ellingwood, Stephan O'Brien, and Sajan Kumar for their insights, discussions and constructive criticisms. Many thanks also to Paul Mercure and Juan Gallego for their technical assistance with the computer systems. Lastly, I would like to thank my family and friends for their love and support.

Abstract

Abrégé

Contents

List of Figures

List of Tables

Chapter 1

Introduction

1.1 Gamma Ray Astrophysics

Gamma ray astrophysics studies the physics and the sources of particles at high energies (E >1 GeV). While astronomy is a centuries-old science, gamma-ray astrophysics has only come into play since the advent of satellite technology and subsequently of Imaging Atmospheric Cherenkov Telescopes (IACTs) in the 1980s. Due to constraints from atmospheric interactions, direct detection of high energy emissions is not feasible with traditional ground-based instruments. However satellites are able to circumvent these issues, and IACTs are able to use them to their benefit.

High-energy (HE, E >1 GeV) or very high energy (VHE, E >100 GeV) gamma-ray emission is a signature of extreme astrophysical processes like relativistic jets and strong electromagnetic fields. These processes are among the most energetic phenomena in the universe and are present in active galactic nuclei (AGN), pulsar wind nebulae (PWN), and pulsars. Since the penetration depth for higher energy photons in the atmosphere is shorter than their optical counterparts, they become much harder to manipulate using conventional methods like those used for photons. Instead, methods of high-energy particle physics and detector technology used for other high-energy particles are used for gamma-ray detection. Satellite-based instruments like the Fermi Large Area Telescope (LAT) are able to detect lower-energy gamma rays (30 MeV – 100 GeV) directly through tracking pair production e^{+}/e^{-} pairs, but for very high energy (VHE) gamma rays (E$>$ 100 GeV) the much lower photon flux means that effective areas required for significant statistics are much larger, and not feasible for satellite-based instruments.

1.1.1 Ground Based Gamma-Ray Astrophysics

The Whipple Collaboration pioneered the technique for indirect detection of gamma rays through the collection of Cherenkov photons emitted from extensive air showers generated from high-energy photon interactions with the atmosphere. The direction of the primary photons can be determined by imaging the air showers with telescopes. This also enables the rejection of hadronic showers from cosmic rays and provides an effective area much larger than is possible with space-based instruments. Cherenkov light used to detect these showers arrives in a region with a radius of $\sim$ 100 m. The current generation of IACTs uses multiple telescopes which provide better sensitivity, better hadronic rejection and larger effective areas than individual telescopes[1]. In the thirty years of ground-based gamma ray astrophysics, over 200 VHE sources have been detected.

The current generation of ground based gamma-ray observatories includes three major telescope arrays. The MAGIC array, located on the Canary Islands of La Palma, Spain consists of two IACTs with 17 m diameter reflectors. The H.E.S.S. array in the Khomas Highlands of Namibia, is an array of five IACTs, four of which have 13 m diameter reflectors while the fifth, in the center of the array has a 28 m reflector. The VERITAS array in Arizona, US, the subject of this thesis, is an array of four telescopes, each with reflectors 12 m in diameter.

1.2 VERITAS Overview

The Very Energetic Radiation Imaging Telescope Array System (VERITAS) is an array of four IACTs at the Fred Lawrence Whipple Observatory in southern Arizona, which started operating in 2007. Gamma rays are detected through imaging Cherenkov radiation emitted from relativistic charged particles (primarily e^+/e^-) in air showers initiated by VHE gamma rays. This section contains a brief description of the instrument and the technique used in this experiment. After the moving of one telescope in 2009, and upgrading the camera to higher quantum efficiency photo-multiplier tubes (PMTs) in 2012, VERITAS is sensitive to an energy range between ~ 85GeV and ~ 30TeV and has a field of view of 3.5°.

Figure 1.1: Photograph of the VERITAS telescopes and the control center. Photo taken from [2].

1.2.1 Gamma-Ray Initiated Extensive Air Showers

At gamma-ray energies, photons interact with the upper atmosphere resulting primarily in pair production of e^+/e^- pairs as shown in Fig. 1.2. On propagating through the atmosphere, electrons/positrons undergo “bremsstrahlung” and emit gamma rays. “Bremsstrahlung”, German for “breaking radiation”, is a process where a charged particle (in this case an electron/positron) accelerated in the electromagnetic field of a nucleus loses energy by emitting photons. The bremsstrahlung photons can again undergo pair production and the shower continues as before resulting in an exponentially growing number of particles, with a decreasing mean particle energy.

Higher energy particles are beamed more strongly forward and so in the VHE gamma-ray energy scale, the particle shower has a small footprint ($\sim$ 30 m) transverse to the direction of the initiating particle, and a large longitudinal distribution ($\sim$ 10 km). As the shower proceeds, the mean energy of the particles gets progressively smaller, due partly to division among a larger number of particles and partly due to loss to ionization. Eventually, the process reaches an energy where Compton scattering becomes the dominant process causing energy loss, and the cascade stops. At this point, the shower energy dissipates into the atmosphere through ionization. Since the cascade which was so far growing exponentially halts here, the number of particles does not increase beyond this point and this point is referred to as the shower-maximum.

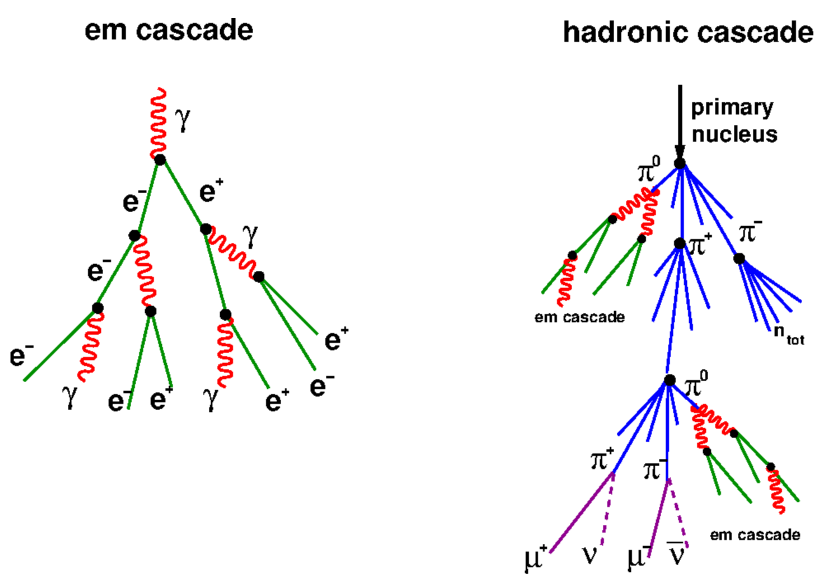

Figure 1.2: Processes involved in generating extensive air showers [3].

1.2.2 Cherenkov Radiation

Cherenkov radiation is electromagnetic radiation emitted by a dielectric medium when a charged particle travels through it at a speed faster than the speed of light in the medium. The mechanism is commonly described as the analog of a sonic boom and the resulting shock wave front. Cherenkov radiation, when intense, appears as a bluish glow like that noticed in the pools of water shielding some nuclear reactors. The phenomenon was experimentally studied by the Soviet physicist Pavel A. Cherenkov in 1934 and was explained by Ilya M. Frank and Igor Y. Tamm in 1937.

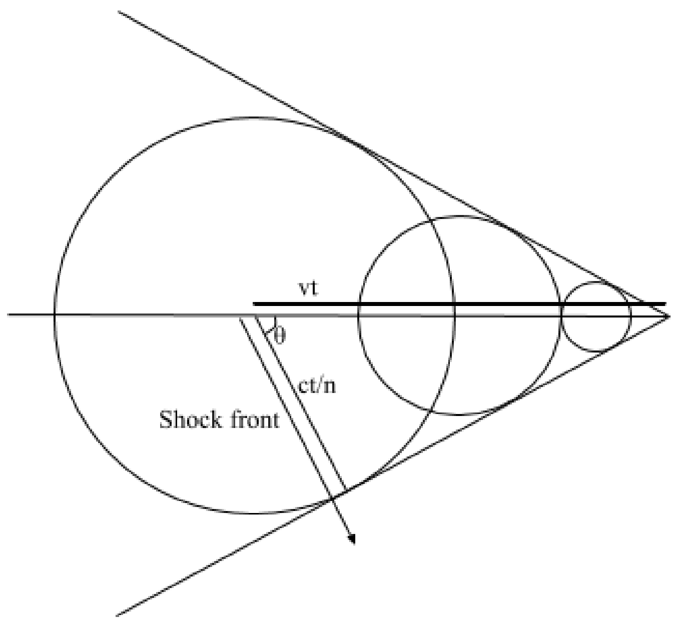

Figure 1.3: Mechanism of Cherenkov radiation.

The speed of light in a medium is given by c/n where n is the refractive index of light in the medium. When the speed of the particle exceeds this speed ($v > c/n$), a shock front appears between the region where an electric field due to the charged particle is present and one where it is not because the electric field can only propagate at the speed of light in the medium (c/n). The shock front travels at an angle given by $\theta = \cos^{-1}(c/vn) = \cos^{-1}(1/\beta n)$ with radiation emitted in a cone with angle θ from the direction of propagation of the initiating charged particle as shown in Fig. 1.3. The number of photons per unit length of particle path per unit of wavelength is given by

$$\frac{d^2N}{dxd\lambda} = \frac{4\pi^2 z^2 e^2}{hc\lambda}\left(1 - \frac{1}{n^2\beta^2}\right) = \frac{2\pi z^2}{\lambda^2}\alpha \sin^2\theta_C \tag{1.1}$$

The inverse dependence on the wavelength means that the photons radiated are mostly on the low-wavelength end of the spectrum. Since Cherenkov radiation is a coherent process, the electric field is perpendicular to the surface of the emission cone and the emission is completely polarized.

1.2.3 Imaging Atmospheric Cherenkov Telescopes

Imaging atmospheric Cherenkov telescopes (IACTs) detect the light produced in an extensive air shower (EAS) by the primary particle. EAS emit a cone of forward-beamed Cherenkov photons with a half-opening angle of $\sim 1^\circ$ [4]. This beam illuminates an elliptical region on the ground called the light pool which has an area of the order of 10^5 m^2, with variations depending on the altitude of the shower maximum and inclination of the shower axis.

The Cherenkov technique resolves (in space and time) the shower development image captured by the telescope camera. This information is used to distinguish between different types of showers (hadronic vs γ-ray-initiated) by using the different spatial spread of the showers depending on initial particles. In particular, for VHE γ-ray showers, because the shower is compact in the transverse direction the direction of the ensuing shower is roughly along a cone with the thickness of the cone inversely dependent on the energy.For hadronic showers, the initial interactions lead to a less compact spread in direction of the resulting particles.

Modern IACTs use multiple telescopes operating in conjunction, which increases

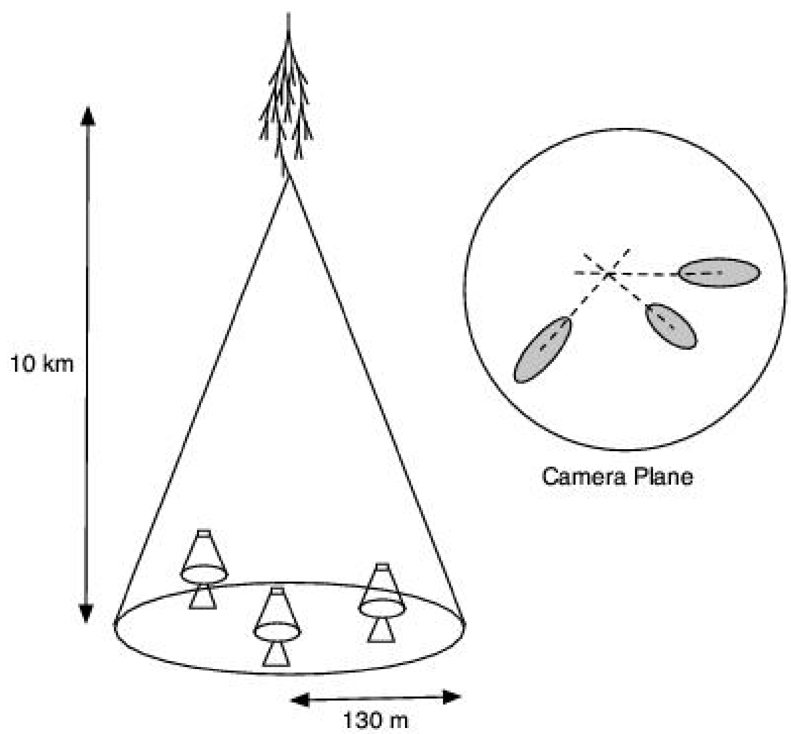

Figure 1.4: Illustration of an IACT array, with typical shower height and radius of light pool for γ-rays with primary energy > 100 GeV. Picture taken from [2].

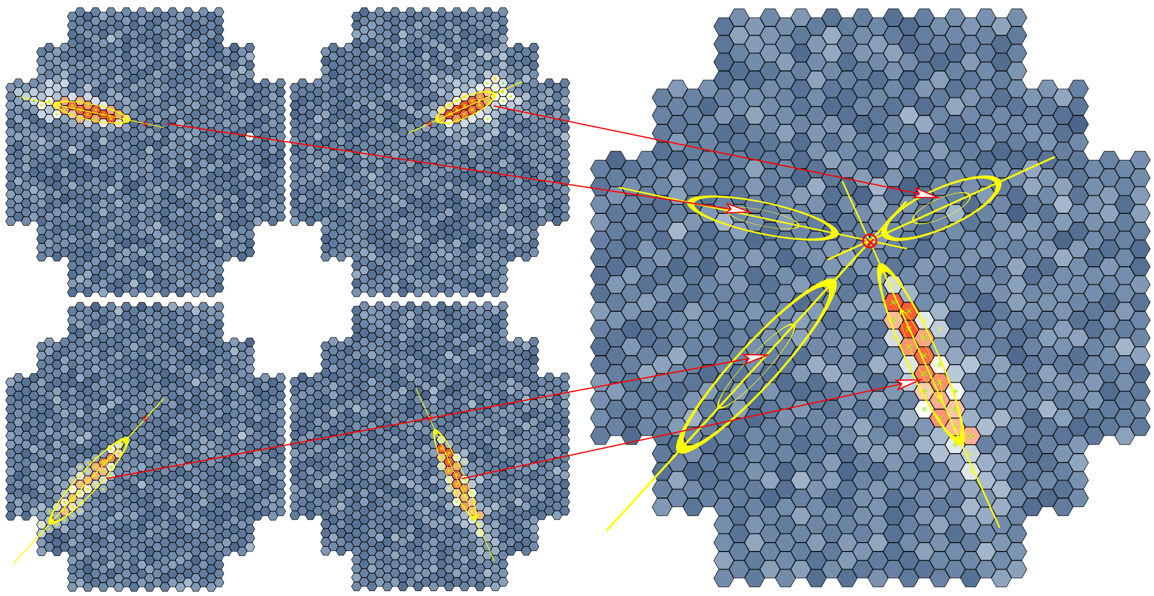

Figure 1.5: Gamma-ray induced air shower incident at a telescope array (left). Image of an air shower on the camera plane. Each telescope image is characterized by an ellipse (right).

effective area as well as directional resolution. Combining the images from the different telescopes enables stereoscopic imaging allowing for reconstructing the axis of the air shower as shown in Fig. 1.4. The majority of EAS are generated by high energy cosmic rays, composed primarily of protons and nuclei, rather than gamma rays. The dominant interactions of these protons – nuclear hadronic interactions – are the same process commonly seen in particle colliders, producing showers dominated by high energy π mesons (π^0, $\pi^{\pm}$).

1.2.4 The VERITAS Instrument

The VERITAS instrument consists of four telescopes, each consisting of a reflector, a camera box, and a counterweight. The reflectors on each telescope are 12 m diameter spherical Davies-Cotton mirrors [5]. The four telescopes are arranged in order to maximize collection area while being close enough for multiple telescopes to fall within the light pool for an air shower. Having multiple telescopes within the light pool allows for better stereoscopic reconstruction as demonstrated in Fig. 1.5. The distance between adjacent telescopes is ~ 100 m and the radius of the light pool for energies > 100 GeV is ~ 130 m.

Each VERITAS telescope uses 345 identical hexagonal spherical mirrors (of area 0.322 m^2 and radius-of-curvature of approximately 24m) giving a total reflector area of nearly 110 m^2. The hexagonal shape allows for more efficient packing of mirrors on the reflector surface.

The individual hexagonal mirrors need to be manually aligned so that the entire reflector will act as a single dish. The measure of the alignment of these mirrors is the point spread function (PSF), which describes the response of the detector to a point source at infinity. The better aligned the system, the smaller the value of the resulting PSF.

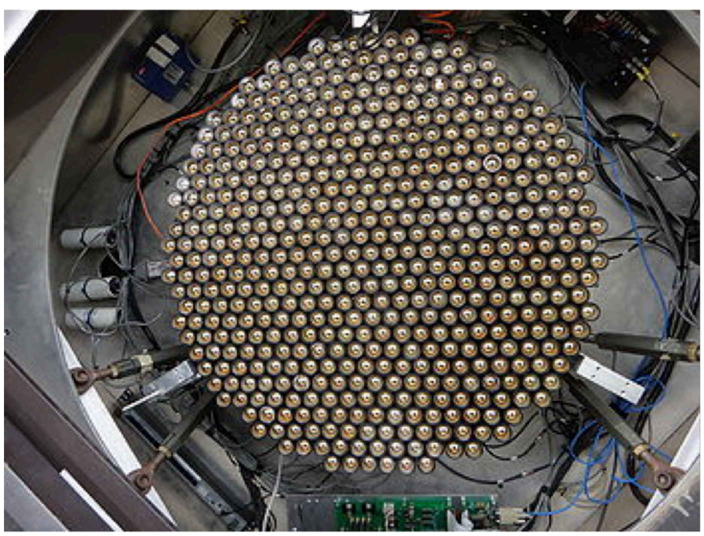

Figure 1.6: The PMT "pixels" in the VERITAS Camera. Picture taken from [6]

The camera in a VERITAS telescope is located at the focal plane of the telescope (12 meters from the mirrors) in a "focus box" of dimension 1.8m x 1.8m. The camera consists of 499 closed-packed circular photomultiplier tubes (PMTs, see Fig. 1.6), giving an angular pixel spacing of 0.15 degree and a total field-of-view (FOV) of 3.5 degrees. The PMTs are arranged in a hexagonal pattern to maximize coverage.

At the low end of the VERITAS energy range, fluctuations in the night sky background (NSB) and (single) muons from cosmic-ray showers constitute a large fraction of the observed single-telescope events. VERITAS employs a three-tier trigger system to reduce the rate of these background events. The first trigger system works on the single-pixel level, the second checks for specific patterns of single level pixels within a timing window, and the third works at the array level, requiring simultaneous observations of an air-shower event in multiple telescopes (ensuring a "stereoscopic" view of the event). The three trigger levels are designated L1, L2 and L3.

The L1 trigger, which is the pixel-level trigger system, has constant fraction discriminators (CFDs) and threshold discriminators for each PMT in the telescope cameras. This trigger requires the signal from a PMT channel to be above a particular threshold, reducing contamination from the night sky background and electronic noise. This information is then passed on to the L2 trigger.

The L2 trigger, reduces effects from NSB and electronic noise by requiring correlations between adjacent pixels. Specifically, this trigger only triggers an output pulse when several adjacent pixels surpass the L1 discriminator threshold within some coincidence window (about 6 ns). The L3 trigger uses this to determine whether to store the data.

Relativistic muons in the atmosphere radiate Cherenkov radiation and comprise a large background source for Cherenkov telescopes at low energies. Muons decaying close to a telescope face produce rings in the camera, but these rings will only be large enough for detection by a single telescope. With this in mind, the L3 trigger is an array-level trigger which depends on receiving telescope level triggers from more than one telescope. Effective removal of the muon background allows sensitivity to the lower energy range where these backgrounds would otherwise dominate.

1.3 Shower Image Parameters

The shower image parameters are the input to the direction reconstruction that is the focus of this work. In any given telescope, the shower image is parameterized using various measurements including

- the image axis – defined as the line minimizing the signal-weighted sum of squares of perpendicular distance between triggering pixels (see 1.3).
- the time gradient – a measure of the difference in time of arrival, along the image axis, of the signal at a pixel (see 1.8).
- the length of the image (see 1.9) – the r.m.s spread of the signal-weighted triggered pixels parallel to the image axis [7].
- the width of the image (see 1.9) – the r.m.s spread of the signal-weighted triggered pixels perpendicular to the image axis. The length and width together provide the major and minor axis of an ellipse containing the majority of the signal, and are referred to as the Hillas parameters and the Hillas ellipse.

A number of other parameters are used in the complete reconstruction of the shower, but these are the most relevant to the direction reconstruction, and specifically to the direction reconstruction process using the boosted decision tree (BDT) angular reconstruction.

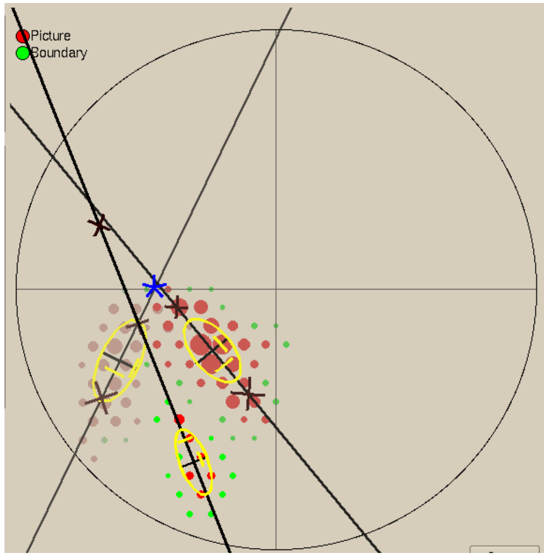

Figure 1.7: The image axis parameter is the line of best fit for the shower image on a single telescope. This best fit is measured by minimizing the signal-weighted sum of squares of residuals. Picture taken from [2].

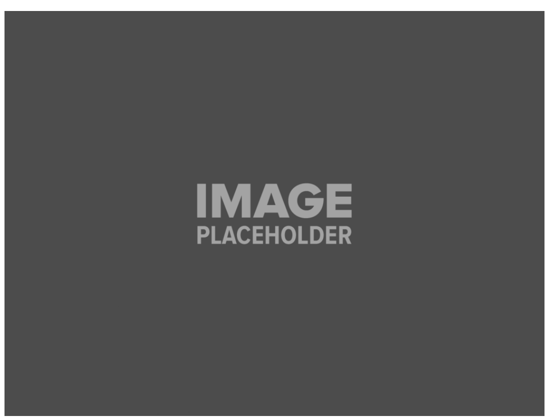

Figure 1.8: Time gradient parameter for a shower.

1.3.1 The *Disp* Parameter

The *Disp* parameter is a measure of the displacement between the center of the Hillas ellipse (the center of gravity of a shower image at a telescope), and the origin of the shower in the camera plane (Fig. 1.10). This is a telescope-level parameter with a head-tail ambiguity, but with multiple telescope images, it can be used in estimating the direction of the initiating gamma ray. This is based on the idea in method (c) described in Hofmann[8].

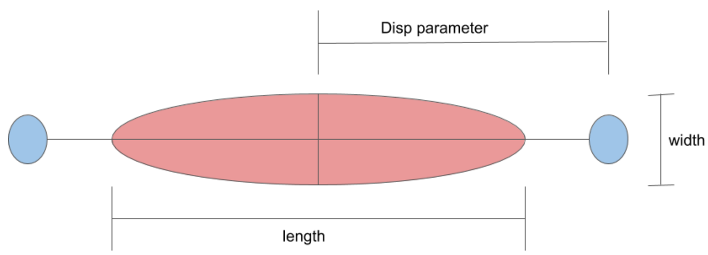

Figure 1.9: Hillas Ellipse (red), with the major axes and the estimated or calculated location of the origin of the shower in the camera plane (blue).

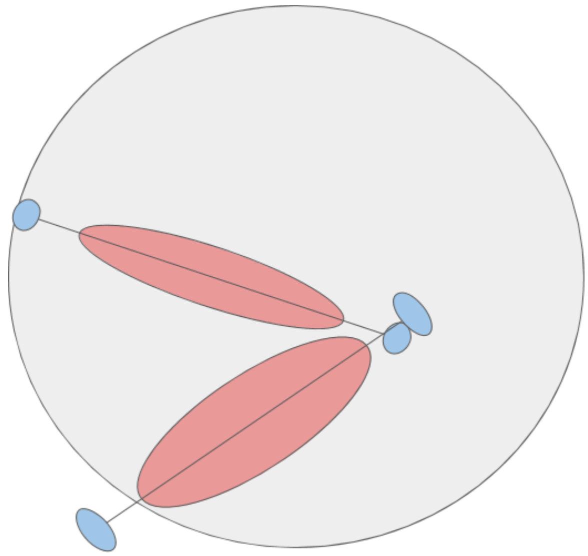

Figure 1.10: The Hillas ellipses (see Fig. 1.9), as used to reconstruct shower direction. In a single telescope image, there is an ambiguity in the direction of the displacement from the center of gravity of the image. However, in a multi-telescope array this ambiguity can be resolved by looking at several Hillas ellipses in conjunction and minimizing the location of the shower source.

Chapter 2

Simulation and Analysis Packages

2.1 Overview

A large number of charged cosmic ray events are included among the triggering events despite the three-level trigger. Most current generation experiments use analysis techniques based on [7], using the second moments of the distribution of pixel signal amplitudes, which for VERITAS, yield an angular resolution of $\sim< 0.1^\circ$ at 1 TeV. However, significantly more information can be extracted from the recorded data using a template library containing expected shower images for a given set of shower parameters. This template library can then be compared to the recorded images for any given event and the best-fit shower parameters can be determined resulting in improved resolution in direction and energy reconstruction. This section provides a brief overview of the Monte-Carlo simulations used to generate these templates for VERITAS.

2.2 Shower Generation

This section describes the prediction of the expected Cherenkov light distribution in the camera focal plane for a given set of primary particle parameters. The production of mean shower images is divided into two steps: the generation of large Monte Carlo datasets of air showers and the simulation of the detector response. The electromagnetic air showers in the atmosphere are simulated with the CORSIKA (COsmic Ray SImulations for KAscade) program and simulations are performed over a range of parameters like energy, zenith angle and impact distance.

In the simulation, which contains the shower generation from 1.2.1, when a charged particle exceeds $v > c/n$, Cherenkov photons are generated. The number of photons emitted is calculated for a given extent of the path and the propagation directions are randomly selected from the surface of a Cherenkov cone (i.e. $\theta_c = \cos^{-1}\beta/n$). Each photon is then tracked through the atmosphere until it reaches the altitude of the observatory. CORSIKA does not track whether the photon hits a telescope reflector, but instead defines a volume around each telescope in order to filter photons to store. Photons whose trajectory does not intersect this volume are not stored.

With the camera pointing at the shower source, each of the telescope cameras lies on a plane perpendicular to the shower axis, making the shower projection plane and the camera planes parallel. The CORSIKA simulation output contains the photon distribution at the telescope altitude, and the arrival direction of each photon. For each event, the Cherenkov photons falling onto the mirror elements are tracked by their arrival times, initial direction, and wavelength. The detector response is modeled using the atmospheric density profile, optical absorption and some of the detector characteristics such as its light-collecting area, and phototube quantum efficiency. It also accounts for the physical structure of the telescopes such as occultation by the quadripod arms and the camera box. The images are produced for the VERITAS telescopes which use a Davies-Cotton design and cameras with 499 pixels, each pixel having a field of view (FOV) of $0.15°$ in diameter.

The shower images are generated for a range of first-interaction depths, energies, wobble offsets and impact distances. A multidimensional interpolation algorithm is used to interpolate between the templates, allowing production of an image template for any shower parameters within the parameter ranges. An additional parameter included here is the effect of the geomagnetic field on the electromagnetic showers [9]. Once the full set of templates has been created, they can be compared with the observed images by performing a global fit to the telescope image data using a model for the expected pixel amplitudes. Shower parameters are determined by maximizing an array likelihood function outlined in [10].

2.3 The VEGAS Analysis Package

The VERITAS observation and simulation data contain the PMT pulses, pointing direction, time and time gradient (which are extracted from the PMT pulses), and other trigger and operational conditions. To produce a sky map, these data files are piped through a series of functions to extract, among other things, energy and direction information. At VERITAS there are two standard analysis packages for this process (*VEGAS* and *EventDisplay*), both based in ROOT/C++, with a similar set of functions. While the analysis methods in this work can be and are applied in both analysis packages, the analysis in this work was performed using the *VEGAS* package. *VEGAS* consists of 6 distinct processes, initially written as 6 distinct modules, as follows:

- Stage 1: Calibration Calculation – This stage calculates the hardware dependent parameters of the VERITAS data and collects relevant information at each trigger level (pixel, telescope, and array) to determine a set of calibration parameters. The following stages can then use these parameters in conjunction with the data to remove any hardware dependence.

- Stage 2: Calibration Application – This stage calculates calibrated charge information for PMT traces using information on pedestals, relative gains, and relative channel timing. In more recent iterations, the analysis module for stage 2 also performs the functions previously performed in stage 3.

- Stage 3: Image Parameterization – This stage removes noisy pixels using stage 1 & 2 information and calculates the image parameters (described in 1.3). This stage treats each telescope independently and so image parameters are calculated for each telescope image.

- **Stage 4: Shower Reconstruction** – This is the most important stage for the purposes of this work. This stage performs an array-level reconstruction of the shower, using individual telescope information to calculate **shower direction**, event energy, depth of the shower maximum, and core location.

- Stage 5: Event Selection – This stage is designed to apply cuts to events based on the output of the previous stages to better distinguish hadronic showers from gamma-ray showers, as well as enforce any other restrictions on telescope-image or stereoscopic parameters.

- Stage 6: Results Extraction – This stage calculates and displays the final results of the desired analysis – single telescope analysis, stereoscopic analysis, spectral analysis or temporal flux analysis.

The focus of this work will be on the direction reconstruction part of stage 4.

2.4 Direction Reconstruction

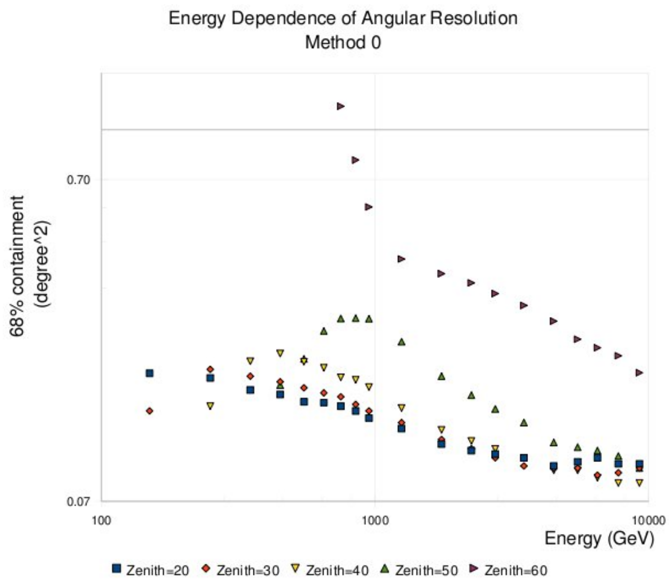

Figure 2.1: Angular resolution of Method0 direction reconstruction against energy scale and zenith angle. Picture taken from [2].

The standard method (henceforth method0) of shower direction reconstruction is based on the intersections of the major axes of Hillas ellipses. This method carries a lot of stereoscopic information and is in general very powerful. However, for large zenith angles (LZA), one expects shower images (and therefore Hillas ellipses) in the camera plane to be from the same region in the lightpool (see Fig. 2.2). close to parallel, small uncertainties in major axis determination result in large uncertainties in the fiducial location of the reconstructed gamma ray in the camera plane (the “shower location”). As shown in Fig. 2.1, for lower energies and larger zenith angles, there is a substantial drop in angular resolution.

To compensate for this loss of predictive power, the *Disp method*, calculates the *Disp* parameter (quasi-analytically, using lookup tables and interpolating, or using **boosted decision trees**) for each individual telescope image to determine two

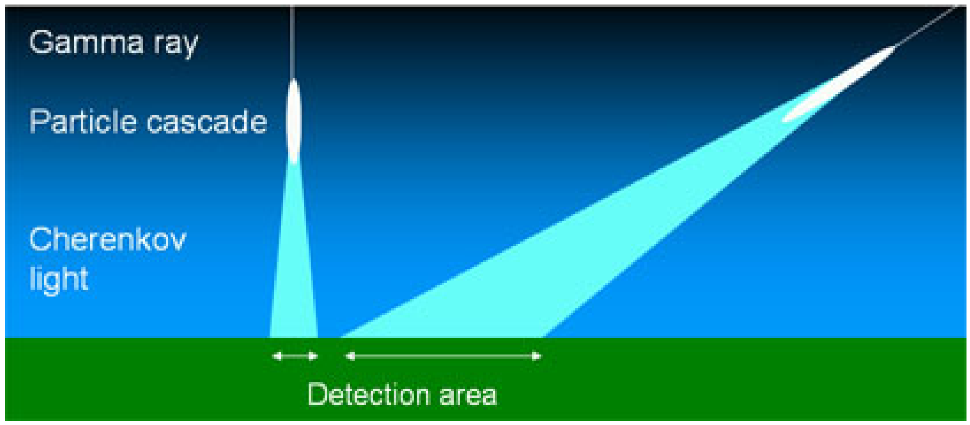

(a) The light pool for Cherenkov showers at small zenith angle versus at large zenith angle. Picture taken from [11].

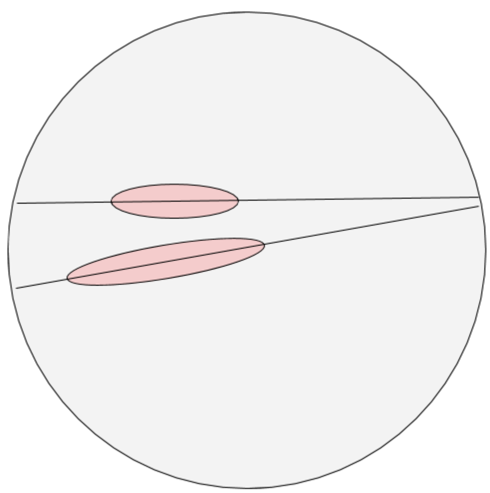

(b) The Hillas ellipses resulting from two telescopes at LZA.

Figure 2.2: The stereoscopic method is less effective at large zenith angles due to the lightpool from these events being much larger than the coverage of the telescopes. This results in the telescopes being in the same region of the light pool and therefore nearly parallel Hillas ellipses. In such cases, the stereoscopic method of reconstruction will have a large uncertainty in the point of intersection of these two axis, which corresponds to a large uncertainty in the reconstructed direction.

potential locations for the arrival direction – along the major axis on either side of the weighted centroid of the image (see Fig. 1.9). The method then compares this pair of coordinates (one at the head, and one at the tail) for each pair of telescopes in the event reconstruction to find the pair of coordinates, one from either telescope, closest to each other (see Fig 2.3 for visual explanation). The mean of this pair of coordinates is determined to be the reconstructed shower direction.

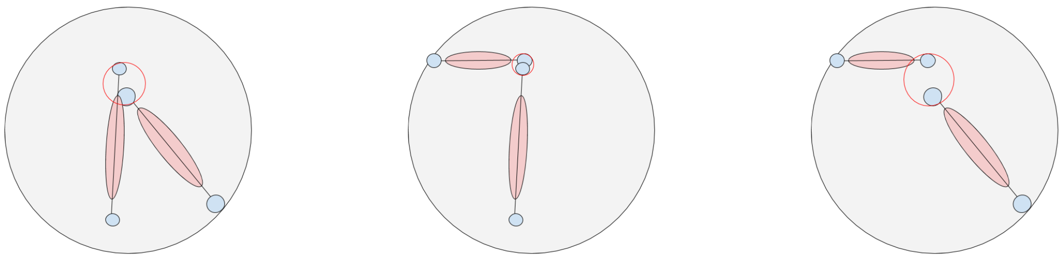

(a) First pair of telescopes in reconstruction, with the pair of closest coordinates.

(b) Second pair of telescopes in reconstruction, with the pair of closest coordinates.

(c) Third pair of telescopes in reconstruction, with the pair of closest coordinates.

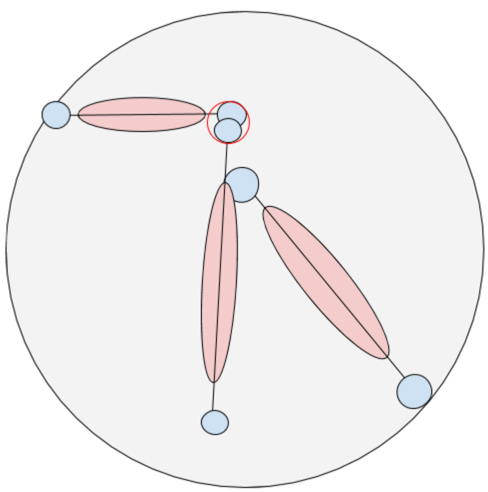

(d) All telescopes in reconstruction, with the pair of closest coordinates from *all* pairs of telescopes.

Figure 2.3: Iterating through the unique pairs of telescopes, the closest coordinate pair is chosen, and the mean of those coordinates is determined to be the direction of the initiating particle.

2.5 Boosted Decision Trees

Decision trees use a predictive model, which maps parameters for an event to the value of the *Disp* parameter for the event. The predictive model may be based on Monte Carlo simulations (as in the case of this work) or analytic calculations. A basic algorithm for boosted decision tree (BDT) learning takes an input sample of data, generates a decision tree, uses a boosting algorithm to better discriminate mis-modeled inputs, and runs tests to provide some measures of it's own performance. BDTs are especially robust for variables with non-linear correlations and have a fast application to data, relative to some of the other algorithms. This section contains a brief description of these individual steps.

2.5.1 Training

Decision trees are a type of supervised learning algorithms. For our purposes, this means the algorithm is provided with a training sample comprised of the values of the parameters used for the reconstruction of each event along with the true value (from simulations) of the parameter to be reconstructed. The training process then generates the correlation matrices for the dependent variables. With this information the algorithm is able to create a decision tree where each non-leaf node denotes a test on an attribute and each branch represents an outcome of the test, at each step using a test that best splits the input data.

2.5.2 Boosting

To avoid having multiple identical trees, a higher weight is assigned to events that are canonically hard to discriminate. This means that within the training, more time is spent on discriminating between events that are hard to distinguish and this assigning of weights to preferentially train more on specific parts of parameter space is referred to as boosting.

2.5.3 Testing

The implementation of the *Disp* method in *VEGAS* (and *EventDisplay*) uses the ROOT Toolkit for Multi-Variate Analysis (TMVA) package. The TMVA package contains implementations of several complex algorithms including neural networks, Fisher discriminants and boosted decision trees (BDTs). The TMVA package contains a built-in testing step to measure certain parameters to help determine the goodness of the training. This step is used to measure deviations of the reconstruction of the testing data-set and the training data-set. A large difference between the performance on the training and testing sets could mean the method has been trained on noise in the training data-set rather than on relevant parameters. This misinterpretation of noise in the training sample as relevant effects is referred to as *overtraining*.

2.6 Noise in Simulations

The night sky background (NSB) level is also a priori expected to influence the reconstruction efficiency. A higher level of NSB photons increases the threshold needed to remove background photons, thereby causing a greater loss of lower energy gamma rays. This decreases the sensitivity to lower energy photons and affects the gamma-ray effective area.

To incorporate this effect in the simulations, gamma-ray shower simulations are created with multiple different noise levels. For the purposes of this work, simulations with noise levels of 200, 250, 300, 350, and 450 MHz were used. These values should accurately recreate the NSB levels at VERITAS observations.

Chapter 3

Analysis Methods

3.1 Preliminary Test and Motivation

The first part of this work was to examine the stability of the reconstructed Crab spectrum looking at the photon index and the integral flux above a threshold value based on the lowest energy where photons were reconstructed across zenith angles. The data used were from nights of horizon-to-horizon Crab runs (Jan 12 2018, Jan 13 2018, and Jan 04, 2019), where Crab runs were taken from the horizon to culmination and back to the horizon.

For Method0, the reconstructed energy spectra appear to be largely stable under variations in zenith angle (Fig. 3.1(a) and 3.1(b)). The slopes of the best fit gradient lines are insignificant for both the integral flux above the threshold energy ($10^{0.35} \approx 2.24$TeV) and the spectral index – as they should be since physically these quantities are independent of zenith angle.

The *Disp* method is able to reconstruct events down to larger zenith angles than the standard method although lower statistics at large zenith angles lead to larger uncertainties. However, the integral flux from the *Disp* method fit has a significant positive correlation with zenith angle, and lies significantly below the integral flux reconstructed from Method0.

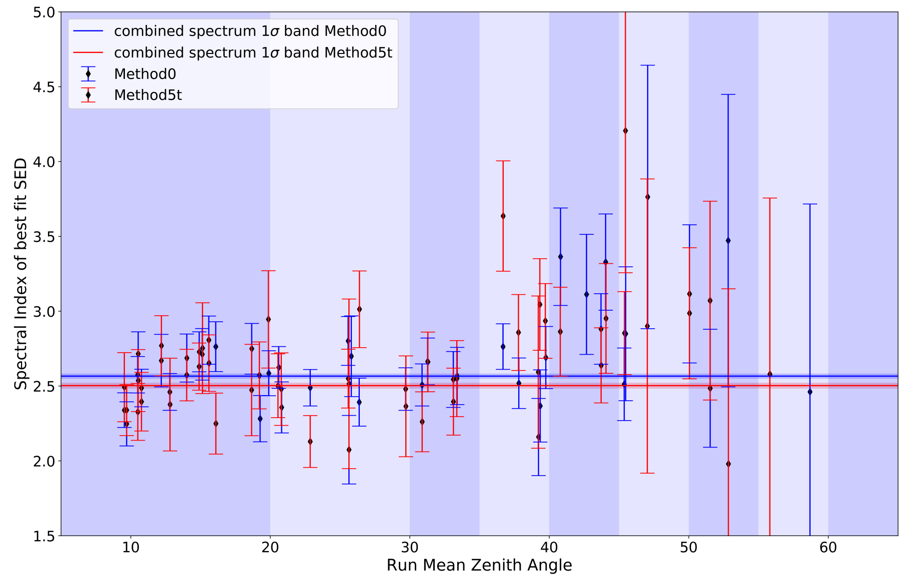

(a) Crab reconstructed spectral index using Method0 and Method5t.

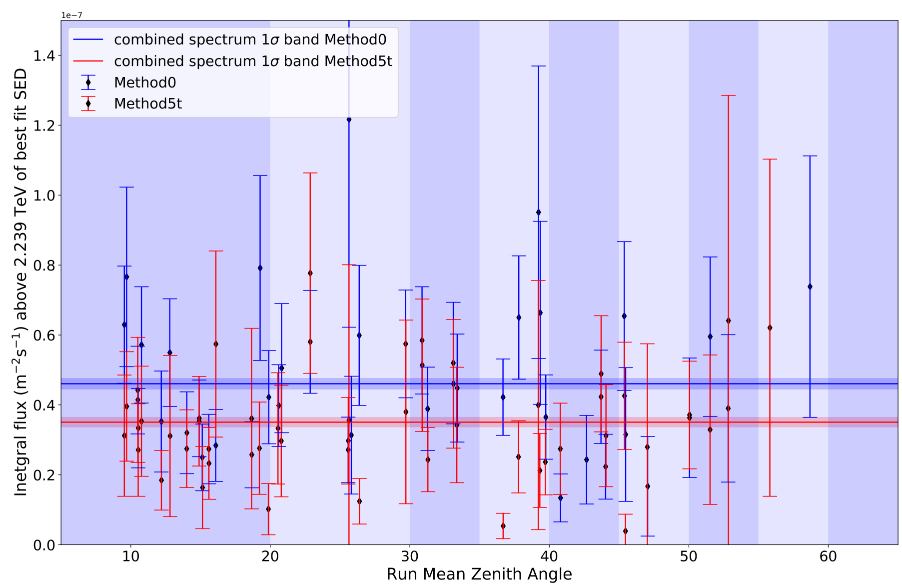

(b) Crab reconstructed integral flux above 2.24 TeV ($10^{0.35}$ TeV) using Method0 and Method5t.

Figure 3.1: Reconstruction of the Crab spectrum using Method0 (standard reconstruction from *VEGAS*) and Method5t (*Disp*).

3.2 *Disp* Table Dependencies

This effect in integral flux hints at some systematic effects that are not yet understood. In order to determine and/or resolve the underlying causes, the scripts to generate the BDT weight tables were re-written and the tables generated independently.

3.2.1 Zenith Angle Dependence

A set of *Disp* tables was generated with a small sample of events ($n \approx 1.9 \times 10^6$) across the range of zenith angles ($20° - 65°$). This was compared to the regular *Disp* method. Since there was no record of the training sample size for the standard tables, this test sample was useful in determining the resolution of the *Disp* method with a relatively small computational footprint. Additionally, it allowed for some simple tests of dependence of the *Disp* table on parameters not explicitly in the *Disp* tables.

The test *Disp* table and the standard *Disp* tables were used to reconstruct simulation events and compared with Method0 (the standard method of direction reconstruction). In both cases, the *Disp* method performs better than Method0 at the largest zenith angles ($\geq 55°$), but the test *Disp* table fared 30-50% worse across zenith angles, and for zenith angles in the range $45° - 50°$, Method0 performed better than the test model. Since the 68% containment tracks the statistical uncertainty of the *Disp* reconstruction (see Fig. 3.2-3.5), this suggested that a larger sample size might be used to improve the angular resolution.

3.2.2 Over-training

BDT based regression is quite robust under non-linear correlations between discriminating parameters, however the primary vulnerability of this method, is that to

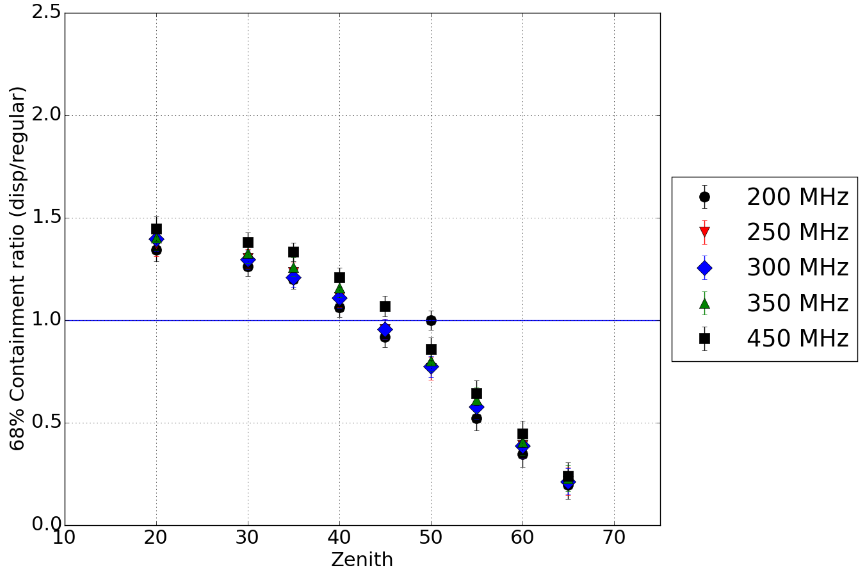

Figure 3.2: Ratio of 68% containment of the "standard" *Disp* table to that from Method0.

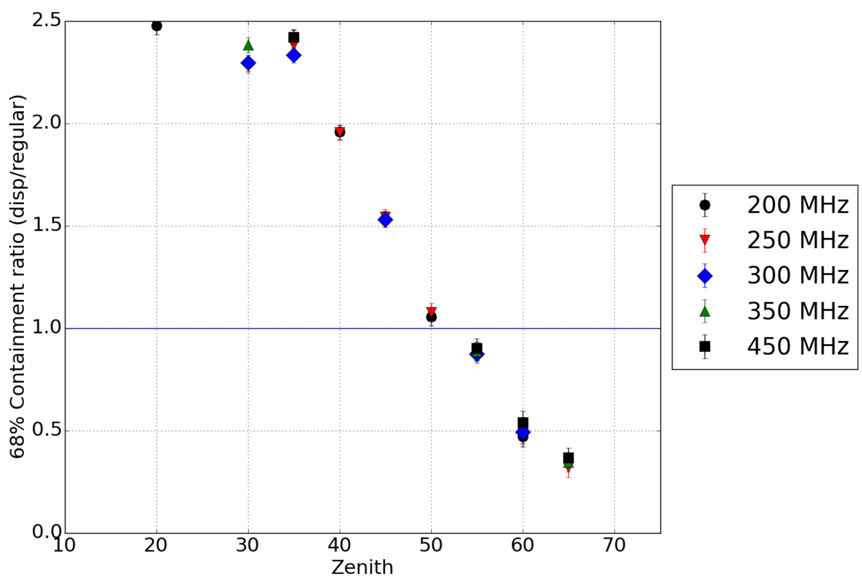

Figure 3.3: Ratio of the 68% containment from reconstruction using test *Disp* table ($\sim 1.9 \times 10^6$ events all at noise = 250 MHz) and that from Method0.

over-training - where the decision tree starts to be informed by noise and nuisance parameters in the training sample rather than relevant effects. This results in substantially different reconstruction efficiencies between training and testing samples. The ROOT TMVA package has a built-in test for over-training where it randomly selects a given fraction of the supplied events (for the purposes of this work, this fraction was taken to be 50%) to use for testing. These events are then not used to train the regression trees and are instead used only to generate a measure of the over-training. This check of the over-training for one of the test tables (noise = 450 MHz), shown in Fig. 3.4, demonstrates that there was no meaningful over-training of the table at least based on effects in the training sample.

There remains however, the possibility of effects related to noise level that might appear in the training *and* testing samples (which are generated separately at each noise level), but not in observational data sets, which would be overlooked by this measure of over-training.

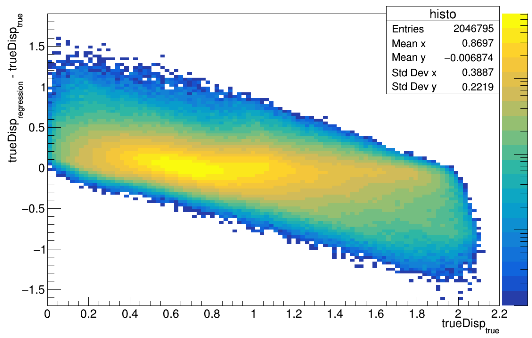

(a) Deviation of reconstructed *Disp* parameter from Monte-Carlo *Disp* parameter in training sample.

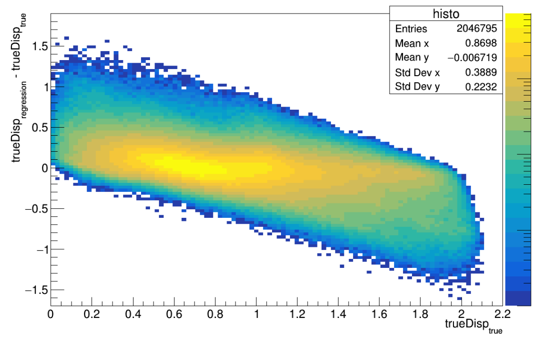

(b) Deviation of reconstructed *Disp* parameter from Monte-Carlo *Disp* parameter in testing sample.

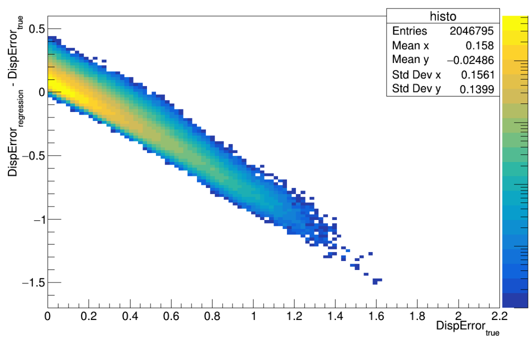

(c) Deviation of reconstructed *Disp* Error parameter from Monte-Carlo *Disp* Error parameter in training sample.

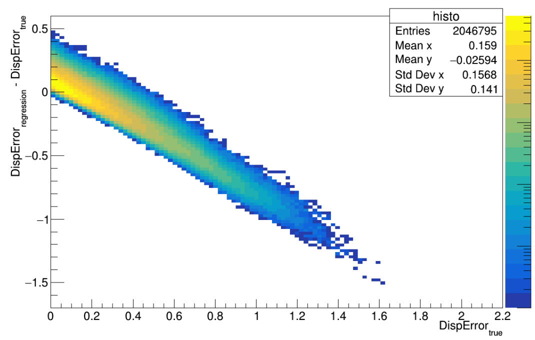

(d) Deviation of reconstructed *Disp* Error parameter from Monte-Carlo *Disp* Error parameter in testing sample.

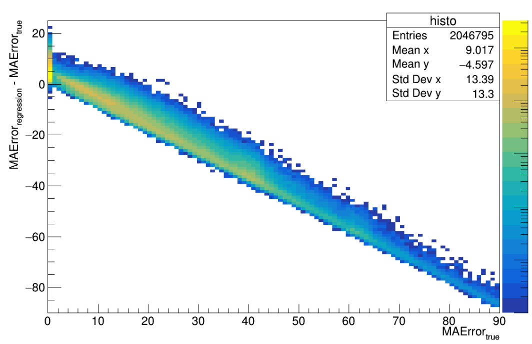

(e) Deviation of reconstructed MAError parameter from Monte-Carlo MAError parameter in training sample.

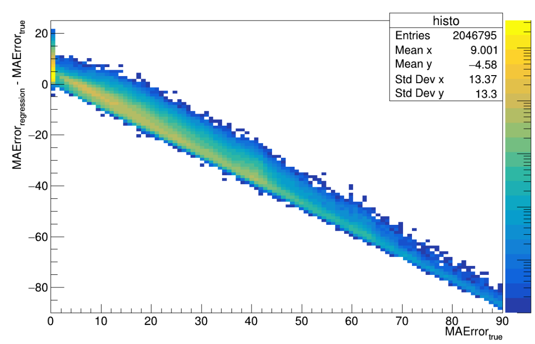

(f) Deviation of reconstructed MAError parameter from Monte-Carlo MAError parameter in testing sample.

Figure 3.4: Over-training check on reconstruction using a *Disp* table generated at a single noise level. The left column shows the deviation of the reconstructed parameter from the true value in the training sample and the column on the right shows the same in the testing sample. The difference between the two columns is small which suggests there is little or no overtraining.

3.2.3 Noise Related Effects

The first set of *Disp* tables was also generated at a single noise level (250 MHz), allowing us to test the dependence of the resolution of this method (as measured by 68% containment) on noise level – some kind of noise-dependent effect would suggest over-training that would not be evident from the testing sample in the ROOT TMVA method since all the data provided to the package would have been at the same noise level. A comparison of angular resolution across noise levels revealed no significant dependence of the 68% containment on noise (see Fig. 3.2, 3.3 and 3.5).

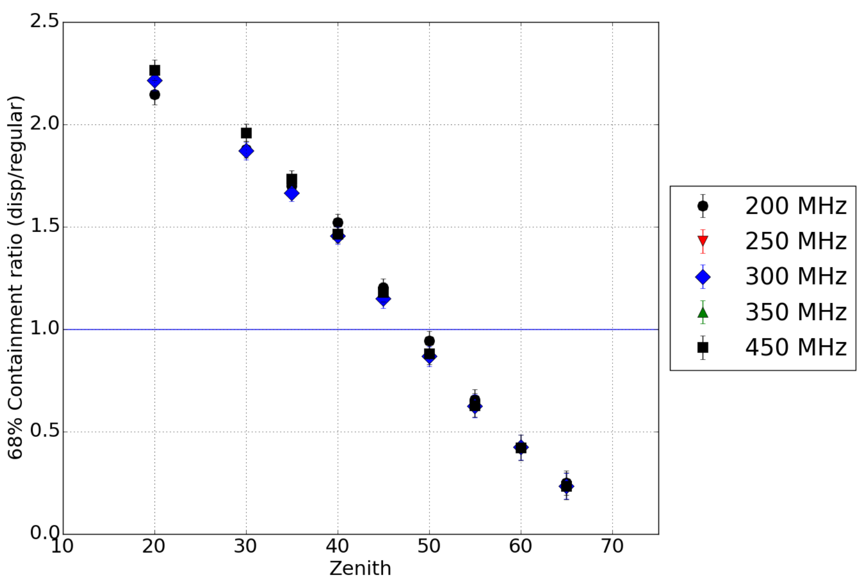

Figure 3.5: Ratio of 68% containment of the noise=450MHz *Disp* table ($\sim 2.1 \times 10^6$ events) to that from Method0.

A second set of test *Disp* tables was generated using a single noise level (noise = 450 MHz) to test for noise-related over-training (see Fig. 3.5). These tables performed slightly better than the first test tables and comparably to the standard *Disp* tables. Since the noise-related effects did not seem to play a significant role in reconstruction, noise was dropped as a discriminating parameter for further analysis.

To generate a set of *Disp* tables with better angular resolution (as measured by 68% containment), another set of *Disp* tables was trained on a larger number of simulations across zenith angles (as before) as well as across the noise spectrum.

3.2.4 Higher Statistics Tables

Once it was determined that there was no significant over-training in the small sample *Disp* tables, and the noise level had little bearing on the 68% containment measure of the reconstruction, it was determined that different noise level simulation events could be used as independent training events to have a higher statistics *Disp* table, and make small improvements on the statistical uncertainty on the reconstruction. The simulation data from across the noise spectrum and zenith range was used to generate a *Disp* table that sampled the entire parameter space more exhaustively.

A new set of *Disp* tables was generated with a training sample four times that of the initial test tables. The improvements in resolution due to change in sample size were modest, and confined to the range of zenith angles where the standard method outperforms the *Disp* method quite considerably.

3.2.5 Acceptance Correction for Offset from Camera Center

Showers arriving further from the camera center have a larger fraction of the shower arriving outside of the camera and therefore being lost. These showers are therefore reconstructed with a lower efficiency and resolution than showers arriving closer to the camera center. To compensate for this in the BDT training, so that the training sample does not mis-characterize the overabundance of events closer to the camera center as an anisotropy in incoming gamma rays, we fold in an acceptance correction by assigning a larger weight to events that are further away from the camera center.

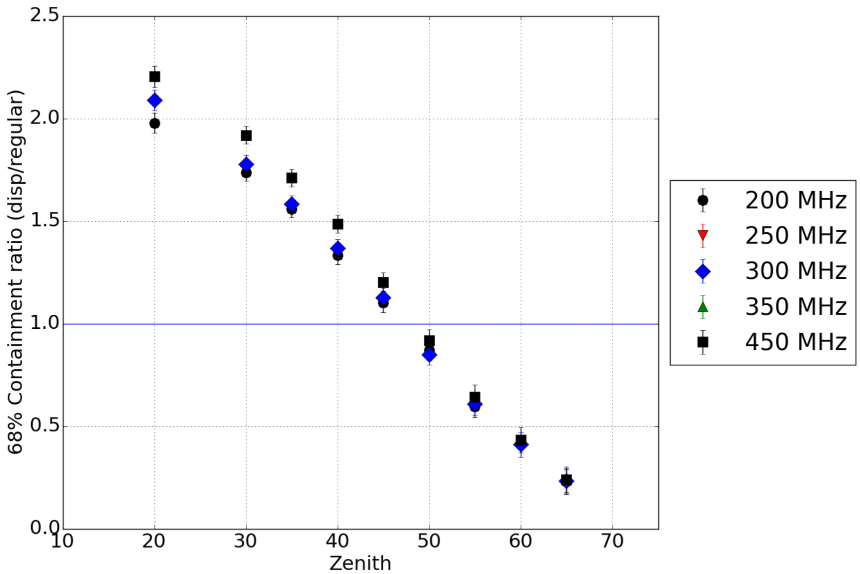

Figure 3.6: Ratio of 68% containment of the noise=450MHz *Disp* table ($\sim 8.4 \times 10^6$ events) to that from Method0 for a higher statistics *Disp* table.

The acceptance correction used here affects the training sample and therefore might be assumed to affect the resolution in a zenith dependent way, explaining the difference in performance between the new *Disp* tables and the old ones. This was tested by using a number of different correction functions in the training sample, as shown in Fig. 3.7

These tests reveal small changes in the 68% containment value despite large changes in the correction function (Fig. 3.8). This suggests that the *Disp* tables are not sensitive to changes in acceptance and therefore the different acceptance functions are unlikely to be the reason why the new *Disp* tables perform worse at smaller zenith angles.

3.2.6 Energy Dependence

Another important dependence of the reconstruction resolution (and therefore the 68% containment) is that on energy. Higher energy photons are expected to comprise a large

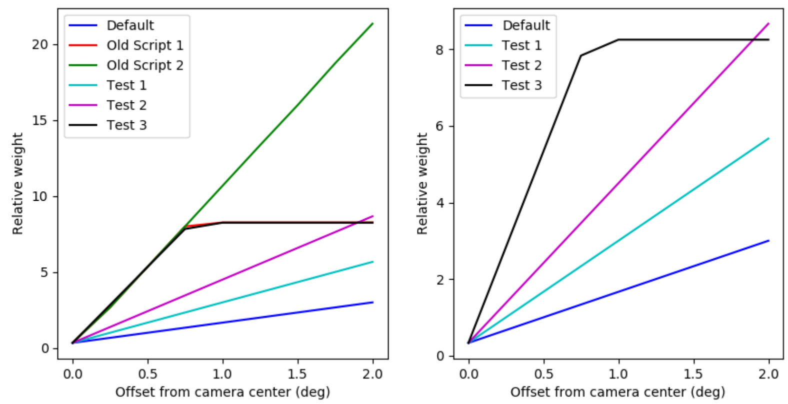

Figure 3.7: The weight functions used in the training samples in the new tables (Default, Test 1, Test 2 and Test 3) and those found in the scripts used to generate the older tables (Old Script 1, Old Script 2).

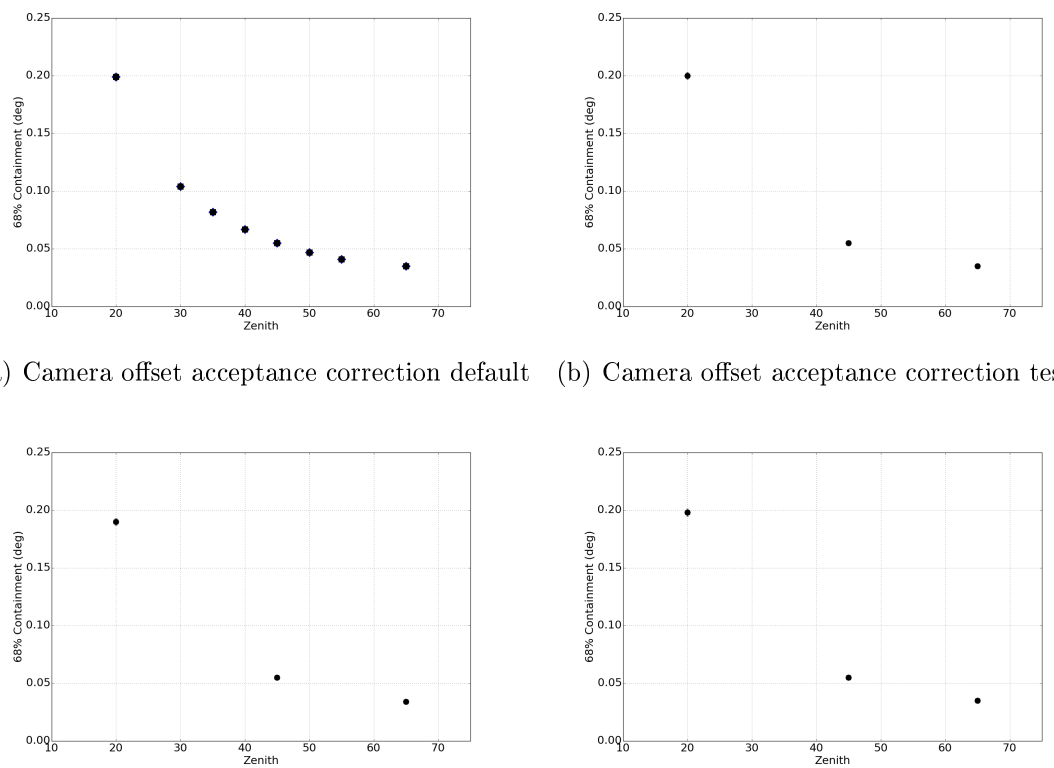

(a) Camera offset acceptance correction default (b) Camera offset acceptance correction test 1

(c) Camera offset acceptance correction test 2 (d) Camera offset acceptance correction test 3

Figure 3.8: 68% containment for each acceptance correction function shown in Fig. 3.7. The changes in acceptance correction do not meaningfully change the 68% containment for the reconstruction.

fraction of all LZA photons which have to travel through longer through the atmosphere and therefore must have showers that remain above the threshold energy deeper into the atmosphere. Conversely, high energy photons are expected to make up a small fraction of SZA photons due to the relative overabundance of generating processes as well as the greater relative likelihood of down-scattering than up-scattering.

Bibliography

[1] Nahee Park. Status of ground based gamma-ray observations. *PoS*, ICRC2017:1116, 2018.

[2] VERITAS collaboration. VERITAS website. `https://veritas.sao.arizona.edu/`.

[3] S. Mollerach and E. Roulet. Progress in high-energy cosmic ray physics. *Progress in Particle and Nuclear Physics*, 98:85–118, Jan 2018.

[4] LA Antonelli, P Blasi, G Bonanno, O Catalano, S Covino, A De Angelis, B De Lotto, M Ghigo, G Ghisellini, GL Israel, et al. The next generation of cherenkov telescopes. a white paper for the italian national institute for astrophysics (inaf). *arXiv preprint arXiv:0906.4114*, 2009.

[5] J. M. Davies and E. S. Cotton. Design of the quartermaster solar furnace. *Solar Energy*, 1:16–22, April 1957.

[6] Dave B. Kieda. The Gamma Ray Detection sensitivity of the upgraded VERITAS Observatory. In *Proceedings, 33rd International Cosmic Ray Conference (ICRC2013): Rio de Janeiro, Brazil, July 2-9, 2013*, page 0700, 2013.

[7] A. M. Hillas. Cerenkov light images of EAS produced by primary gamma. *International Cosmic Ray Conference*, 3, August 1985.

[8] W. Hofmann. Data analysis techniques for stereo IACT systems. *AIP Conf. Proc.*, 515(1):318–322, 2000.

[9] Stephane Vincent. A Monte Carlo template-based analysis for very high definition imaging atmospheric Cherenkov telescopes as applied to the VERITAS telescope array. *PoS*, ICRC2015:844, 2016.

[10] Mathieu de Naurois and Loïc Rolland. A high performance likelihood reconstruction of γ-rays for imaging atmospheric Cherenkov telescopes. *Astroparticle Physics*, 32:231–252, Dec 2009.

[11] HESS collaboration. H.E.S.S. website. `https://www.mpi-hd.mpg.de/hfm/HESS/pages/home/som/2005/10/`.